

The role of chalcogen vacancies for atomic defect emission in MoS₂

Elmar Mitterreiter

TUM <https://orcid.org/0000-0002-5314-3238>

Bruno Schuler

Swiss Federal Laboratories for Materials Science and Technology

Katja Barthelmi

Technical University of Munich

Katherine Cochrane

Lawrence Berkeley National Laboratory

Jonas Kiemle

Technical University of Munich

Florian Sigger

Walter Schottky Institut and Physik Department, Technische Universität München

Julian Klein

Technical University of Munich <https://orcid.org/0000-0002-0873-8224>

Ed Wong

Lawrence Berkeley National Laboratory

Edward Barnard

The Molecular Foundry <https://orcid.org/0000-0003-4736-0743>

Sivan Refaely-Abramson

Molecular Foundry, Lawrence Berkeley National Laboratory

Diana Qiu

Yale University

Michael Lorke

University of Bremen

Frank Jahnke

University of Bremen <https://orcid.org/0000-0003-3384-1060>

Kenji Watanabe

National Institute for Materials Science <https://orcid.org/0000-0003-3701-8119>

Takashi Taniguchi

National Institute for Materials Science, Tsukuba, Ibaraki

Jonathan Finley

TU Muenchen

Adam Schwartzberg

Lawrence Berkeley National Laboratory

Alexander Holleitner

Technical University Munich

Alexander Weber-Bargioni

Molecular Foundry-LBNL

Christoph Kastl (✉ christoph.kastl@wsi.tum.de)

Technical University of Munich <https://orcid.org/0000-0001-5309-618X>

Article

Keywords: semiconductors, chalcogen vacancies, MoS₂

Posted Date: November 20th, 2020

DOI: <https://doi.org/10.21203/rs.3.rs-105682/v1>

License:  This work is licensed under a Creative Commons Attribution 4.0 International License.

[Read Full License](#)

Version of Record: A version of this preprint was published at Nature Communications on June 22nd, 2021. See the published version at <https://doi.org/10.1038/s41467-021-24102-y>.

Abstract

For two-dimensional (2D) layered semiconductors, control over atomic defects and understanding of their electronic and optical functionality represent major challenges towards developing a mature semiconductor technology using such materials. Here, we correlate generation, optical spectroscopy, atomic resolution imaging, and *ab-initio* theory of chalcogen vacancies in monolayer MoS₂. Chalcogen vacancies are selectively generated by in-vacuo annealing, but also focused ion beam exposure. The defect generation rate, atomic imaging and the optical signatures support this claim. We discriminate the narrow linewidth photoluminescence signatures of vacancies, resulting predominantly from localized defect orbitals, from broad luminescence features in the same spectral range, resulting from adsorbates. Vacancies can be patterned with a precision below 10 nm by ion beams, show single photon emission, and open the possibility for advanced defect engineering of 2D semiconductors at the ultimate scale.

Introduction

Control over atomic defects is the foundation of today's semiconductor technology. For two-dimensional van der Waals semiconductors, the term "defect engineering" has been coined to suggest that, by introducing defects, these materials can be engineered beyond the established concepts of doping or alloying¹, enabling advanced functionality, such as single photon sources^{2,3} or photocatalysis with chemical specificity¹. Nevertheless, the microscopic understanding of defect-related modifications remains elusive due to a lack of thorough correlation between atomic structure and resulting macroscopic electronic and optical properties. Combining controlled defect engineering with optical spectroscopy as well as atomic imaging and *ab-initio* theory, we identify the optical signature of pristine chalcogen vacancies in MoS₂. Vacancies introduce a deep center with sharp optical emission, markedly different from previously observed broad luminescence bands.⁴⁻⁸ Comparing annealed vs. He-ion treated MoS₂, we establish that the recently discovered single-photon emitters in He-ion irradiated MoS₂ originate from chalcogen vacancies³. The latter can be deterministically created with a precision below 10 nm⁹, underscoring the potential of defect engineering for two-dimensional (quantum-) optoelectronics.

In semiconductors, the interaction of free excitons with the Coulomb potential of lattice defects results in localized defect-exciton complexes¹⁰. In the traditional picture, exciton localization at shallow defects introduces an additional binding energy. Therefore, optical signatures of defects lie energetically below the free exciton¹⁰. Defect levels deep inside the band gap provide further relaxation pathways at even lower transition energies¹⁰. Since in two-dimensional (2D) semiconducting transition metal dichalcogenides, including MoS₂, MoSe₂, WS₂ and WSe₂, the screening of the defect potential is weak, and also the exciton Bohr radius is small ($\sim 2 - 3$ nm)¹¹, excitons are extremely confined in real space when coupling to defects¹². Therefore, as shown theoretically for MoSe₂ and MoS₂, chalcogen vacancy

levels give rise to a series of strongly bound defect excitons which then hybridize with excitonic states of the pristine system^{12,13}.

At low-temperatures, most 2D semiconductors exhibit broad sub-gap emission extending several hundred meV below the exciton^{4,5,7,8,14}. Generally, this sub-gap luminescence becomes stronger with increasing number of point defects present in the TMD layer, and it is often called L-band (emphasizing localization) or D-band (emphasizing defects) in the literature. The correlation between defects and the L-band was found either by introducing additional defects^{5,14} or by correlating spatial fluctuations of the existing defect density and excitonic properties^{4,15}. Nevertheless, there is a surprising lack of consensus about the origin for such broad defect emission. Some studies emphasized radiative recombination at intrinsic point defects as underlying mechanism^{4,7}. Other studies highlighted the relevance of molecular adsorbates. For example, calculations show that adsorbed molecular oxygen modifies the electronic structure of the sulfur vacancy in MoS₂, either by removing the in-gap state¹⁶ or by *p*-doping via hole transfer from oxygen⁶. Furthermore, it has been suggested that laser illumination incorporates atomic oxygen into pre-existing chalcogen vacancies either by photo-assisted dissociation of molecular oxygen¹⁷ or water¹⁸. However, chalcogen vacancies are likely already passivated by atomic oxygen in as-prepared TMDs^{9,19,20}. Moreover, several studies demonstrated that laser annealing in controlled gas environments^{21,22} or encapsulation in hBN²³ can completely remove the L-band suggesting chemisorbed or physisorbed molecules as its origin²².

By contrast, a spectrally sharp sub-gap luminescence and single photon emission was also reported at low-temperatures². As the microscopic model, a combination of strain potentials, which funnel and localize excitons, and atomic defects, which provide recombination centers for localized excitons, was suggested². While these point-like emitters appear randomly in as-prepared samples, they can be generated deterministically via engineered nanoscale strain potentials². Recently, our group has demonstrated that atomic point defects, which are created deterministically by He-ion irradiation⁹, act as narrow and reproducible single-photon emitters, yet without a local strain potential^{3,24}. Here, we disentangle broad defect emission due to adsorbates, which can be desorbed by *in-vacuo* annealing at moderate temperatures, and narrow defect emission *via* sulfur vacancies, which are generated both by annealing at high temperatures and He-ion irradiation.

Results

Figure 1 shows low-temperature photoluminescence (PL) spectra of monolayer MoS₂ on hexagonal boron nitride (hBN). In addition to exciton (⁰X_A) and trion (X_A),¹¹ as-exfoliated MoS₂ exhibits a prominent L-band from approximately 1.5 eV to 1.9 eV (Fig. 1a). Mild annealing ($T_{\text{annealing}} = 500$ K) in vacuum

results in a striking reduction of the L-band (Fig. 1b), presumably due to desorption of adsorbates. Further annealing at high temperature ($T_{\text{annealing}} = 800$ K) introduces a narrow peak X_L at 1.75 eV (Fig. 1c). A similar, yet even sharper, spectral signature is observed in fully encapsulated MoS₂ after He-ion irradiation (Fig. 1d). The improved inhomogeneous broadening agrees with previous studies of fully hBN encapsulated heterostructures²³. In the following, we show that adsorbates introduce a continuum of defect states, which is responsible for the L-band emission, whereas pristine sulfur vacancies introduce a deep center, which is very likely also the origin of recently discovered single photon emission in He-ion treated MoS₂.^{3,24}

Figure 2 shows low-temperature PL of MoS₂ after stepwise *in-vacuo* annealing up to 800 K. In each cycle, the samples were rapidly annealed in a customized cryostat for 30 min and then cooled back to cryogenic temperature ($T_{\text{sample}} \sim 20$ K) for PL characterization maintaining a high vacuum ($p < 10^{-4}$ mbar) at all times (Supplementary Information S1). Figure 2a illustrates spectra of as-exfoliated MoS₂ on hBN and after several mild annealing steps to 420 K, 450 K, and 510 K. Again, the as-exfoliated flake exhibits a prominent L-band (cf. Fig. 1a). The intensity of the L-band decreases relative to the intensity of the free exciton emission by one order of magnitude after annealing to $T_{\text{annealing}} = 420$ K, and it gradually disappears for higher annealing temperatures (Fig. 2b). Furthermore, the trion emission decreases initially compared to the free exciton indicating a reduced doping, as observed previously in TMDs during desorption of physisorbed gas²⁵ and chemical dopants²⁶. Hence, we attribute the L-band to adsorbates, which are progressively removed during the mild annealing steps. The desorption does not follow a simple Arrhenius law, since it depends on the total number of adsorbates, which is unknown. Therefore, we can estimate only an upper bound of ~ 100 meV for the desorption barrier, which agrees with *ab-initio* studies for molecular adsorbates on MoS₂²⁷ and temperature programmed desorption on bulk MoS₂²⁸.

At $T_{\text{annealing}} = 510$ K, a spectrally narrow emission line X_L appears around 1.75 eV. In contrast to the L-band, the intensity of X_L increases with higher annealing temperatures, until the whole PL signal disappears at $T_{\text{annealing}} > 700$ K (see Supplementary Information S2). To extract the thermal activation barrier of X_L , we use an hBN/MoS₂/hBN heterostack, where the L-band is already suppressed in the as-prepared structures. As seen in Fig. 2c, X_L brightens in the encapsulated monolayer with increasing annealing temperature, and further narrows after annealing to 800 K indicating a complete removal of residual adsorbates. At even higher temperatures ($T_{\text{annealing}} = 900$ K), the intensity of X_L decreases drastically, followed by the complete disappearance of the overall PL (Supplementary Information S2). Consistent with saturating a finite density of localized defect levels, X_L exhibits a saturating behavior as function of excitation power (see Supplementary Information S3)²⁴. In a simple rate equation model, the saturated defect emission is then proportional to the total number of emission centers. In this case, we can readily determine the energy barriers for defect generation since it is proportional to the difference in the integrated spectral weight of X_L compared to the previous annealing step. For example, the number of defects generated during annealing at 600 K is proportional to the difference in integrated PL intensity, which we label $\Delta\text{Int}(X_L)$, after annealing to 600 K and 510 K. In the limit of low density, defect generation

is independent of the number of existing defects, and we expect a simple Arrhenius law. From Fig. 2d, we find an activation energy of (0.71 ± 0.13) eV for the X_L -peak consistent with theoretical predictions for the formation energy of mono-sulfur vacancies (approximately 1 eV)^{29,30}. Interstitial sulfur defects should not form under high-vacuum, i.e. sulfur-poor, conditions²⁹. The formation energies for transition metal vacancies are much larger (3 eV – 8 eV)^{29,30}. Consequently, the formation of sulfur vacancies during annealing is thermodynamically the most favorable and, therefore, most likely process.

We continue to corroborate the dominant generation of sulfur vacancies during annealing by atomic-scale characterization. Here, we perform high-resolution low-temperature scanning tunneling microscopy (STM) and atomic force microscopy (AFM) of single-layer MoS₂ before and after high-temperature annealing in vacuum ($T_{\text{annealing}} > 500$ K) as well as before and after He-ion irradiation. These experiments are conducted on graphene/SiC heterostructures. The graphene substrate is essential as conductive support, but it quenches the optical emission from defects (Supplementary Information S7)³¹. For STM, all samples were prepared *in-vacuo* by a mild annealing step in vacuum ($T_{\text{annealing}} < 500$ K) to remove adsorbates. In agreement with our optical studies, the surface of MoS₂ is virtually free from adsorbates after mild annealing. By far the most dominant defects in pristine material were oxygen atoms substituting sulfur, but no sulfur vacancies were observed (Supplementary Information S5)^{9,19,20}.

After additional high-temperature annealing, we observed only two additional types of defects within our experimental statistics (Fig. 3). Their high-resolution STM topography exhibits a trigonal symmetry (Figure 3a and 3b), consistent with a vacancy either in the top or bottom sulfur lattice. For both vacancies, the charge densities calculated by DFT (Supporting Information S7) at a distance of 4.5 Å above the MoS₂ layer (similar to experimental conditions in STM) are shown in Figs. 3c and 3d. The calculations are in good agreement with the STM topography. The top vacancy appears trigonally ring-shaped, whereas the bottom vacancy appears triangular-shaped with bright maxima at the corners. These same defects, i.e. top and bottom sulfur vacancies, were also confirmed in the He-ion irradiated samples (Fig. 3e and Fig. 3f). For He-ion treated samples, sulfur vacancies are the dominant defect type, among other defects that are generated with lower yield⁹. Furthermore, we performed CO-tip AFM on the sulfur vacancies (Figure 3g and Fig. 3h). For the top vacancy, we observe an apparent depression at the sulfur site, whereas for the bottom vacancy structural relaxation results in a slight protrusion, in agreement with previous studies on WS₂²⁰. Most importantly, AFM conclusively assigns the defect onto the sulfur sublattice, which is difficult from STM alone²⁰. Overall, the scanning probe experiments confirm the composition and surface condition of MoS₂ derived from optical characterization (cf. Fig. 1). From our different annealing experiments, we conclude that defect luminescence X_L at 1.75 eV arises from pristine, i.e. undecorated, sulfur vacancies. We note that, there are at least two pathways for formation of sulfur vacancies, which are desorption of a sulfur atom or desorption of an oxygen atom from a sulfur site. The latter substitute for sulfur in as-prepared TMDs^{19,20}. Based on the similarity of the optical spectra and the abundance of sulfur vacancies in thermally annealed as well as in He-ion irradiated MoS₂

(cf. Figure 1), we propose that also the origin of quantum emission from individual He-ion induced defects is due to the (non-passivated) sulfur vacancy²⁴.

From *ab-initio* calculations of defective MoS₂ (5×5 supercell corresponding to 2 % of vacancies), three types of excitonic transitions are qualitatively distinguished, as shown in Fig. 4a. Transitions at the optical gap (X_A) arise mainly from unbound electronic states between valence and conduction band at K and K' valleys. The next series of transitions (D_2) occur predominantly between the resonant defect state overlapping with the valence band and the localized in-gap states. In the dilute limit, the localized defect states are k-independent, such that defect-defect transitions cannot exhibit valley-selectivity¹². The lowest series of transitions (D_1) couples the localized in-gap state to dispersive states in the valence band near K and K', and they are predicted to show valley selectivity. Overall, the strong electron-hole interaction leads to a vast manifold of excitonic transitions for the defective crystal with varying eigen energies and mixed degrees of pristine and defect-like character, and in general many different excitonic states contribute to the absorbance spectrum^{12,13}. Figure 4b compares the absorbance spectrum calculated within the GW plus Bethe-Salpeter equation (GW-BSE) approach^{32,33} and experimental photoluminescence of a MoS₂ monolayer with sulfur vacancies. The calculated sub-gap resonances located about 0.45 eV and 0.3 eV below the free exciton transition (0X_A) can be associated with transitions of type D_1 and D_2 , respectively. We note that the absorbance includes a phenomenological broadening of 0.1 eV, which accounts for the numerical uncertainty of the used approach¹². Furthermore, the localization at the atomic scale defect results in a large spread of the exciton transitions in *k*-space, which further broadens the absorption resonances¹².

For the experimental curves, vacancies were introduced in fully encapsulated MoS₂ both by *in-vacuo* thermal annealing and by *ex-situ* helium ion modification. All spectra are referenced to the neutral exciton transition, where we found 1.89 eV for the calculated spectrum and 1.96 eV (1.94 eV) for the measured annealed (ion-modified) spectrum. Notably, while the dominant defect emission (X_L) occurs about 0.2 eV below 0X_A , we consistently observe weak emission features (red arrows) at even lower energies³. The multiple sub-gap emission peaks are qualitatively in agreement with the *ab-initio* calculations of excitonic defect states (top panel of Fig. 4b). Although absorbance cannot strictly be used to infer emission properties, we identify possible transitions based on the correspondence between calculated absorbance and experimental emission spectrum. Within the computational uncertainty, the defect emission at 1.75 eV agrees with the energy range where calculations predict dominant contributions from defect to defect transitions (D_2). Figure 4c further corroborates this assignment. Here, we plot the emission spectrum of a single defect, which was generated by He-ion bombardment^{9,24}, for co- and cross-circularly polarized excitation and detection. We do not detect a valley polarization, as expected for a transition that occurs between localized defect levels. Therefore, we conclude that the X_L peak observed in our thermally annealed as well as He-ion treated MoS₂ monolayers arises due to a localized excitonic transition between the defect orbitals of the pristine sulfur vacancy.

Typically, the dominant emission process should involve the lowest energy state of the system, i.e. transitions of type D_1 . However, in our experiments, the defect emission is governed by transitions of intermediate energy, i.e. transitions of type D_2 , although the calculated oscillator strength varies only weakly in the relevant regime. A naïve scenario to explain our observations involves a relaxation cascade after the absorption process: optical excitation creates a free exciton, which gets localized, and then both hole and electron decay into a defect state (type D_2). If further relaxation of the captured exciton into an excitonic state of type D_1 is slow or prohibited, the emission will occur dominantly from the fully localized electron and hole state. From a theory point of view, the above picture demands to include further interactions, such as exciton-exciton or exciton-phonon coupling³⁴.

In summary, by combining far-field optical spectroscopy, atomic-resolution scanning probe microscopy, and *ab-initio* theory, our study provides compelling evidence of optical defect emission from pristine sulfur vacancies in single layer MoS_2 . In contrast to previous studies, these pristine sulfur vacancies are generated *in-vacuo* or capped by hBN, and therefore, neither passivated by oxygen nor decorated with adsorbates. Similar to previous reports, we observe a broad L-band luminescence due to adsorbates in as-prepared MoS_2 monolayers, which can be suppressed by a combination of h-BN encapsulation and mild annealing. In as-prepared layers and after mild annealing, pristine sulfur vacancies are absent, and oxygen passivated vacancies are the dominant defect. We suggest that oxygen-passivated vacancies form active sites for adsorption of molecular species, since many previous studies established a positive correlation between sulfur deficiency and defect emission^{4,5,15}. Pristine vacancies are created in h-BN/ MoS_2 /h-BN heterostructures either via *in-vacuo* thermal annealing or *ex-situ* helium ion bombardment, whereby the latter allows generating single photon emitters on demand²⁴ with a position accuracy below 10 nm⁹. Guided by *ab-initio* calculations, we identify transitions between a localized in-gap defect state and a localized resonant defect state as the most likely candidate.

Methods

Sample preparation. We micromechanically exfoliated MoS_2 (SPI Supplies) and hBN (NIMS, K.W. and T.T.) using adhesive tape. We used an all-dry viscoelastic stamping technique to transfer single flakes to a substrate consisting of SiO_2/Si or epitaxial graphene on (6H)-SiC using a polydimethylsiloxane (PDMS) stamp. During the transfer, we heated the samples to approximately 60°C, to increase the transfer probability. We cleaned the samples with acetone, isopropanol, and nitrogen gas after each stacking step to remove residues and increase the adhesion.

In-vacuo annealing. We annealed all samples in a modified optical cryostat (Janis ST-500). A customized heater was added to the cryostat for rapid thermal cycling between cryogenic temperatures ($T_{\text{sample}} \sim 20$ K) and high temperatures ($T_{\text{sample}} \sim 900$ K). We determined the annealing temperature at the sample with a thermocouple. We rapidly ramped to the desired annealing temperature and kept it constant for 30

minutes, then we cooled the sample with the highest possible rate back to cryogenic temperatures and conducted the PL measurements.

Photoluminescence spectroscopy. The annealed samples were studied with a custom microscope set-up ($\lambda_{\text{excitation}} = 532 \text{ nm}$, Nikon Plan Fluor ELWD 20x/0.45, WD 7.4 mm). The cryostat was mounted on a motorized xy-stage (ASI) with a minimum stepsize of 100 nm. The emitted light was focused onto the entrance slit of the spectrometer (Andor Kymera 328, grating 300 grooves/mm) and the signal was collected by a CCD camera (Andor iXon). The valley polarization measurements of the ion-treated samples were carried out in He-flow cryostat at $T = 10 \text{ K}$ ($\lambda_{\text{excitation}} = 590 \text{ nm}$, Mitutoyo 100x/0.5 M Plan Apo NIR, WD 12 mm, PI Acton SP-2500i spectrometer, grating 300 grooves/mm). The circular polarization was adjusted using an achromatic $\lambda/4$ -plate in front of the objective lens. The emitted light passed again through the same waveplate, and the polarization was analyzed using a linear polarizer.

Scanning probe microscopy. We performed combined scanning tunneling microscopy and atomic force microscopy (Createc) at low temperatures ($T \sim 6 \text{ K}$) in vacuum with a base pressure of around 10^{-10} mbar. All samples were treated by mild annealing ($T \sim 500 \text{ K}$) under UHV conditions for 10 - 20 minutes. All STM images were recorded using the constant-current feedback and current setpoint of $I_t = 100 \text{ pA}$. Chemically etched tungsten tips were sharpened by repeated indentations into a Au(111) substrate. All AFM images were recorded with a qPlus quartz crystal tuning fork in constant height mode with an applied bias voltage $V_{\text{bias}} = 0 \text{ V}$.

Helium ion microscopy. Single layer MoS_2 flakes supported by graphene/SiC were nanostructured using a helium ion microscope (HIM ORION NanoFab, Zeiss). The whole MoS_2 flake was exposed to a constant helium ion dose of $5 \cdot 10^{14} \text{ cm}^{-2}$. We operated the HIM at a helium pressure of $2.5 \cdot 10^{-6} \text{ Torr}$, a beam energy of 30 keV, beam current of 0.7 pA, pixel spacing of 5 nm, and field of view (FOV) of 100 μm . To obtain the desired constant helium ion dose, the dwell time was adapted to the beam current.

Theoretical calculations. DFT calculations of the defect orbitals in Fig. 3 were performed using the Vienna Ab initio Simulation Package, VASP 5.4.4³⁵. Details can be found in Supplementary information S7. The GW-BSE approach used to calculate the absorbance spectra of MoS_2 with sulfur vacancies in Fig. 4 is described in Supplementary information S8.

References

1. Lin, Z. *et al.* Defect engineering of two-dimensional transition metal dichalcogenides. *2D Mater.* **3**, 022002 (2016).
2. Chakraborty, C., Vamivakas, N. & Englund, D. Advances in quantum light emission from 2D materials. *Nanophotonics* **8**, 2017–2032 (2019).
3. Barthelmi, K. *et al.* Atomistic defects as single-photon emitters in atomically thin MoS₂. *Appl. Phys. Lett.* **117**, 070501 (2020).
4. Carozo, V. *et al.* Optical identification of sulfur vacancies: Bound excitons at the edges of monolayer tungsten disulfide. *Sci. Adv.* **3**, e1602813 (2017).
5. Tongay, S. *et al.* Defects activated photoluminescence in two-dimensional semiconductors: interplay between bound, charged and free excitons. *Sci. Rep.* **3**, 2657 (2013).
6. Nan, H. *et al.* Strong Photoluminescence Enhancement of MoS₂ through Defect Engineering and Oxygen Bonding. *ACS Nano* **8**, 5738–5745 (2014).
7. Greben, K., Arora, S., Harats, M. G. & Bolotin, K. I. Intrinsic and Extrinsic Defect-Related Excitons in TMDCs. *Nano Lett.* **20**, 2544–2550 (2020).
8. Korn, T., Heydrich, S., Hirmer, M., Schmutzler, J. & Schüller, C. Low-temperature photocarrier dynamics in monolayer MoS₂. *Appl. Phys. Lett.* **99**, 102109 (2011).
9. Mitterreiter, E. *et al.* Atomistic Positioning of Defects in Helium Ion Treated Single-Layer MoS₂. *Nano Lett.* **20**, 4437–4444 (2020).
10. Klingshirn, C. F. *Semiconductor optics*. (Springer, 2005).
11. Wang, G. *et al.* Colloquium: Excitons in atomically thin transition metal dichalcogenides. *Rev. Mod. Phys.* **90**, 021001 (2018).
12. Refaely-Abramson, S., Qiu, D. Y., Louie, S. G. & Neaton, J. B. Defect-Induced Modification of Low-Lying Excitons and Valley Selectivity in Monolayer Transition Metal Dichalcogenides. *Phys. Rev. Lett.* **121**, (2018).
13. Bretscher, H. M. *et al.* The bright side of defects in MoS₂ and WS₂ and a generalizable chemical treatment protocol for defect passivation. *ArXiv200203956 Cond-Mat* (2020).
14. Chow, P. K. *et al.* Defect-Induced Photoluminescence in Monolayer Semiconducting Transition Metal Dichalcogenides. *ACS Nano* **9**, 1520–1527 (2015).
15. Kastl, C. *et al.* Effects of defects on band structure and excitons in WS₂ revealed by nanoscale photoemission spectroscopy. *ACS Nano* **13**, 1284–1291 (2019).
16. Gogoi, P. K. *et al.* Oxygen Passivation Mediated Tunability of Trion and Excitons in MoS₂. *Phys. Rev. Lett.* **119**, 077402 (2017).
17. Lu, J. *et al.* Bandgap Engineering of Phosphorene by Laser Oxidation toward Functional 2D Materials. *ACS Nano* **9**, 10411–10421 (2015).
18. Sivaram, S. V. *et al.* Spatially Selective Enhancement of Photoluminescence in MoS₂ by Exciton-Mediated Adsorption and Defect Passivation. *ACS Appl. Mater. Interfaces* **11**, 16147–16155 (2019).

19. Barja, S. *et al.* Identifying substitutional oxygen as a prolific point defect in monolayer transition metal dichalcogenides. *Nat. Commun.* **10**, 3382 (2019).
20. Schuler, B. *et al.* Large Spin-Orbit Splitting of Deep In-Gap Defect States of Engineered Sulfur Vacancies in Monolayer WS₂. *Phys. Rev. Lett.* **123**, (2019).
21. Rogers, C., Gray, D., Bogdanowicz, N. & Mabuchi, H. Laser annealing for radiatively broadened MoSe₂ grown by chemical vapor deposition. *Phys. Rev. Mater.* **2**, 094003 (2018).
22. Venanzi, T. *et al.* Exciton localization in MoSe₂ monolayers induced by adsorbed gas molecules. *Appl. Phys. Lett.* **114**, 172106 (2019).
23. Cadiz, F. *et al.* Excitonic Linewidth Approaching the Homogeneous Limit in MoS₂-Based van der Waals Heterostructures. *Phys. Rev. X* **7**, 021026 (2017).
24. Klein, J. *et al.* Site-selectively generated photon emitters in monolayer MoS₂ via local helium ion irradiation. *Nat. Commun.* **10**, 2755 (2019).
25. Tongay, S. *et al.* Broad-Range Modulation of Light Emission in Two-Dimensional Semiconductors by Molecular Physisorption Gating. *Nano Lett.* **13**, 2831–2836 (2013).
26. Mouri, S., Miyauchi, Y. & Matsuda, K. Tunable Photoluminescence of Monolayer MoS₂ via Chemical Doping. *Nano Lett.* **13**, 5944–5948 (2013).
27. Li, H., Huang, M. & Cao, G. Markedly different adsorption behaviors of gas molecules on defective monolayer MoS₂: a first-principles study. *Phys. Chem. Chem. Phys.* **18**, 15110–15117 (2016).
28. Miremadi, B. K. & Morrison, S. R. Exfoliated MoS₂ Temperature programmed desorption. *Surf. Sci.* **173**, 605–617 (1986).
29. Noh, J.-Y., Kim, H. & Kim, Y.-S. Stability and electronic structures of native defects in single-layer MoS₂. *Phys. Rev. B* **89**, 205417 (2014).
30. Komsa, H.-P. & Krasheninnikov, A. V. Native defects in bulk and monolayer MoS₂ from first principles. *Phys. Rev. B* **91**, 125304 (2015).
31. Lorchat, E. *et al.* Filtering the photoluminescence spectra of atomically thin semiconductors with graphene. *Nat. Nanotechnol.* **15**, 283–288 (2020).
32. Rohlffing, M. & Louie, S. G. Electron-hole excitations and optical spectra from first principles. *Phys. Rev. B* **62**, 4927–4944 (2000).
33. Hybertsen, M. S. & Louie, S. G. Electron correlation in semiconductors and insulators: Band gaps and quasiparticle energies. *Phys. Rev. B* **34**, 5390–5413 (1986).
34. Chen, H.-Y., Sangalli, D. & Bernardi, M. Exciton-Phonon Interaction and Relaxation Times from First Principles. *Phys. Rev. Lett.* **125**, 107401 (2020).
35. Kresse, G. & Furthmüller, J. Efficiency of ab-initio total energy calculations for metals and semiconductors using a plane-wave basis set. *Comput. Mater. Sci.* **6**, 15–50 (1996).

Declarations

Author contributions

E.M., B.S., A.W.-B., A.M.S., A.W.H. and C.K. conceived and designed the experiments. T.T. and K.W. provided hBN crystals. E.M., F.S. and Jo.K. prepared the samples, E.M. and J.K. performed He-ion beam exposure. E.M., K.C. and B.S. performed the STM and AFM experiments. E.M., E.W., E.B. and C.K. carried out annealing and optical experiments. K.B., J.K. and J.J. provided measurements of valley polarization. M.L. and F.J. simulated the DFT wavefunctions, D.Q. and S.R.-A. carried out GW-BSE calculations. E.M., A.W.H. and C.K. analyzed the experimental data and wrote the manuscript with input from all authors. All authors reviewed the manuscript.

Notes

The authors declare no competing financial interest.

Acknowledgements

Work at the TU Munich was supported by Deutsche Forschungsgemeinschaft (DFG) through the German Excellence Strategy via the Munich Center for Quantum Science and Technology (MCQST), EXC-2111-390814868, and e-conversion, EXC 2089/1-390776260. Work at the Molecular Foundry was supported by the Center for Novel Pathways to Quantum Coherence in Materials, Office of Science, Office of Basic Energy Sciences, of the U.S. Department of Energy under contract no. DE-AC02-05CH11231. We gratefully acknowledge support through TUM International Graduate School of Science and Engineering (IGSSE), the Bavaria California Technology Center (BaCaTeC), and Nanosystems Initiative Munich (NIM). J.K. acknowledges support from the Alexander von Humboldt Foundation. K.W. and T.T. acknowledge support from the Elemental Strategy Initiative conducted by the MEXT, Japan, Grant Number JPMXP0112101001, JSPS KAKENHI Grant Number JP20H00354 and the CREST(JPMJCR15F3), JST. M.L. and F.J. acknowledge support from DFG (RTG 2247 Quantum Mechanical Materials Modelling).

Figures

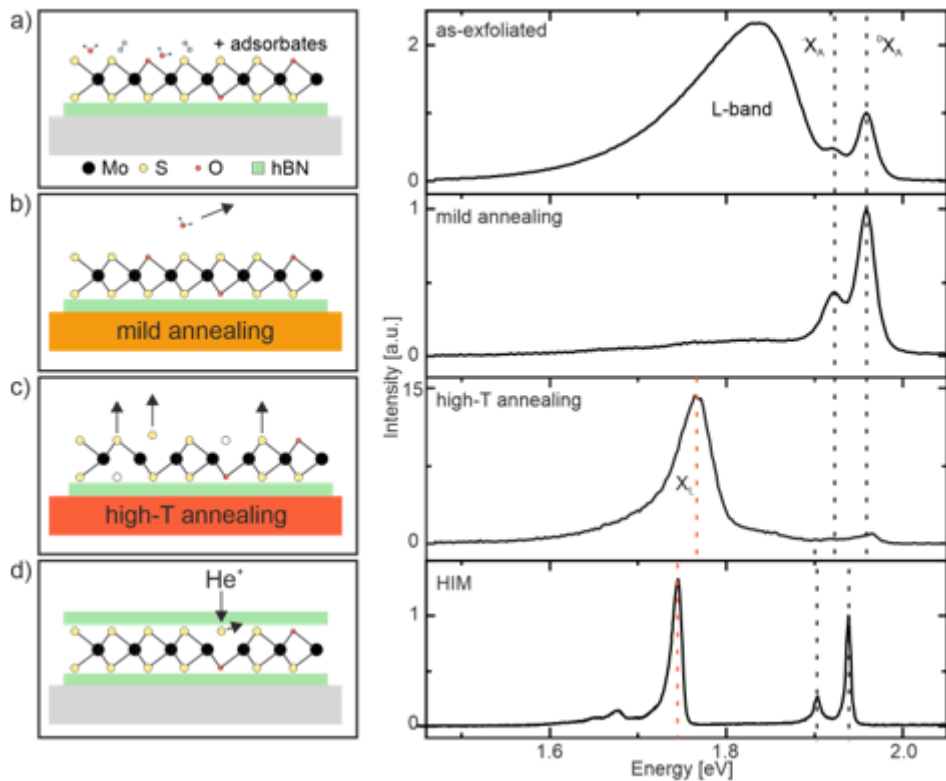


Figure 1

Optical emission induced by adsorbates and engineered point defects in single-layer MoS₂. Schematic of adsorbate removal and sulfur vacancy generation in single layer MoS₂ after in-vacuo thermal annealing (left panel) and evolution of low-temperature ($T \sim 20$ K) photoluminescence spectra (right panel). (a) As-exfoliated MoS₂ exhibits a broad sub-gap luminescence (L-band) due to adsorbates. (b) Mild annealing at $T_{\text{annealing}} = 500$ K removes these adsorbates suppressing the L-band. (c) Upon annealing at $T_{\text{annealing}} = 800$ K, a narrow defect luminescence at 1.75 eV emerges (XL), due to the thermal generation of sulfur vacancies with well-defined in-gap states. Vertical, dashed lines indicate the emission energy of the neutral exciton (0XA), the trion (-XA), and XL. The intensities are normalized to the exciton transition 0XA. (d) Helium-ion irradiated MoS₂ encapsulated in hBN (left panel) exhibits a similar defect feature at 1.75 eV (right panel, $T = 4.2$ K).

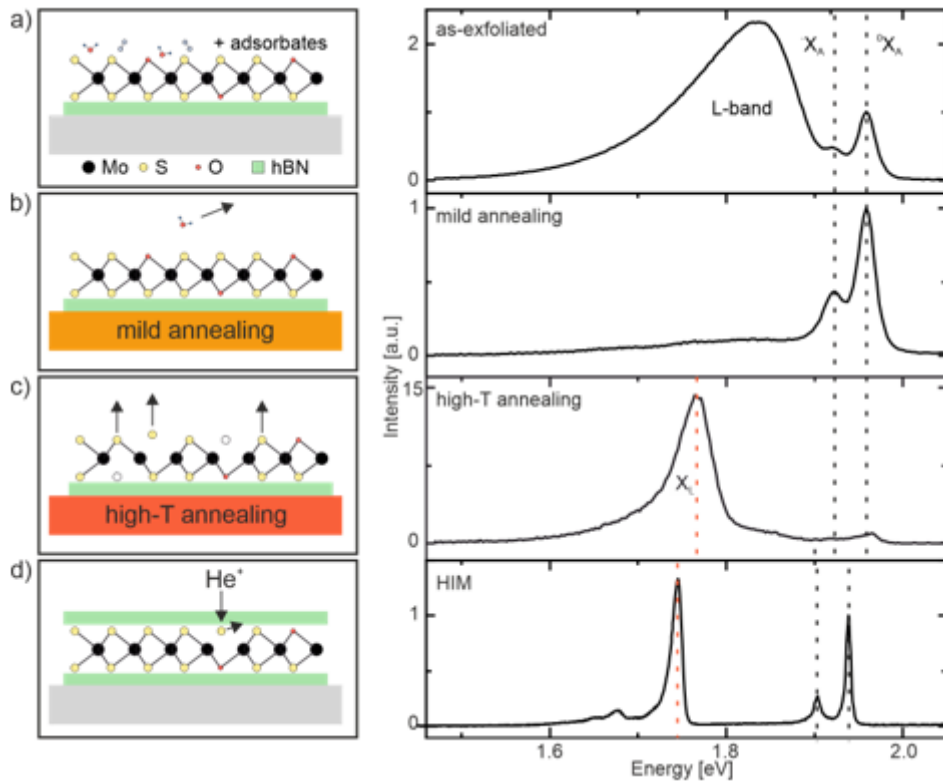


Figure 1

Optical emission induced by adsorbates and engineered point defects in single-layer MoS₂. Schematic of adsorbate removal and sulfur vacancy generation in single layer MoS₂ after in-vacuo thermal annealing (left panel) and evolution of low-temperature ($T \sim 20$ K) photoluminescence spectra (right panel). (a) As-exfoliated MoS₂ exhibits a broad sub-gap luminescence (L-band) due to adsorbates. (b) Mild annealing at $T_{\text{annealing}} = 500$ K removes these adsorbates suppressing the L-band. (c) Upon annealing at $T_{\text{annealing}} = 800$ K, a narrow defect luminescence at 1.75 eV emerges (XL), due to the thermal generation of sulfur vacancies with well-defined in-gap states. Vertical, dashed lines indicate the emission energy of the neutral exciton (0X_A), the trion (-X_A), and XL. The intensities are normalized to the exciton transition 0X_A. (d) Helium-ion irradiated MoS₂ encapsulated in hBN (left panel) exhibits a similar defect feature at 1.75 eV (right panel, $T = 4.2$ K).

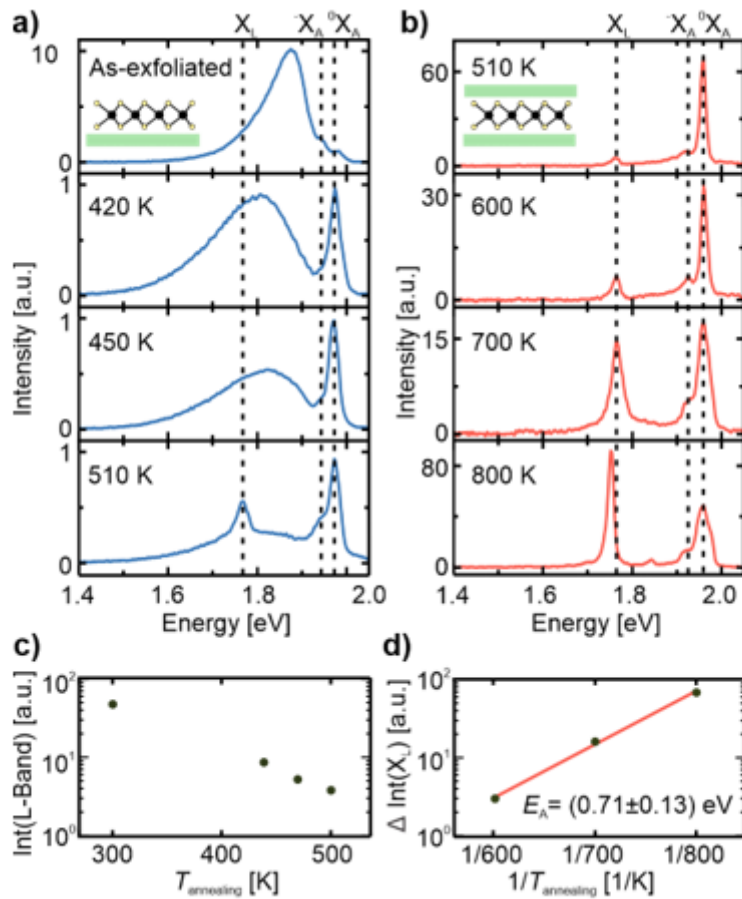


Figure 2

Evolution of MoS₂ low-temperature PL with increasing annealing temperature. a) Compared to as-exfoliated MoS₂ on hBN (top panel) the broad L-band is strongly reduced after successive mild annealing. At 510 K, an emission line XL appears at 1.75 eV (bottom panel). b) PL spectra of fully encapsulated MoS₂. With increasing annealing temperature, the intensity of XL increases. Dashed lines highlight neutral exciton (0XA), trion (-XA), and XL. c) Integrated intensity of the L-band in (a) as function of annealing temperature. The change in L-band emission is related to the desorption rate of adsorbates from the MoS₂. d) Arrhenius plot of thermal defect generation rate extracted from the intensity of XL. The activation barrier is $(0.71 \pm 0.13) \text{ eV}$ consistent with formation of sulfur vacancies.

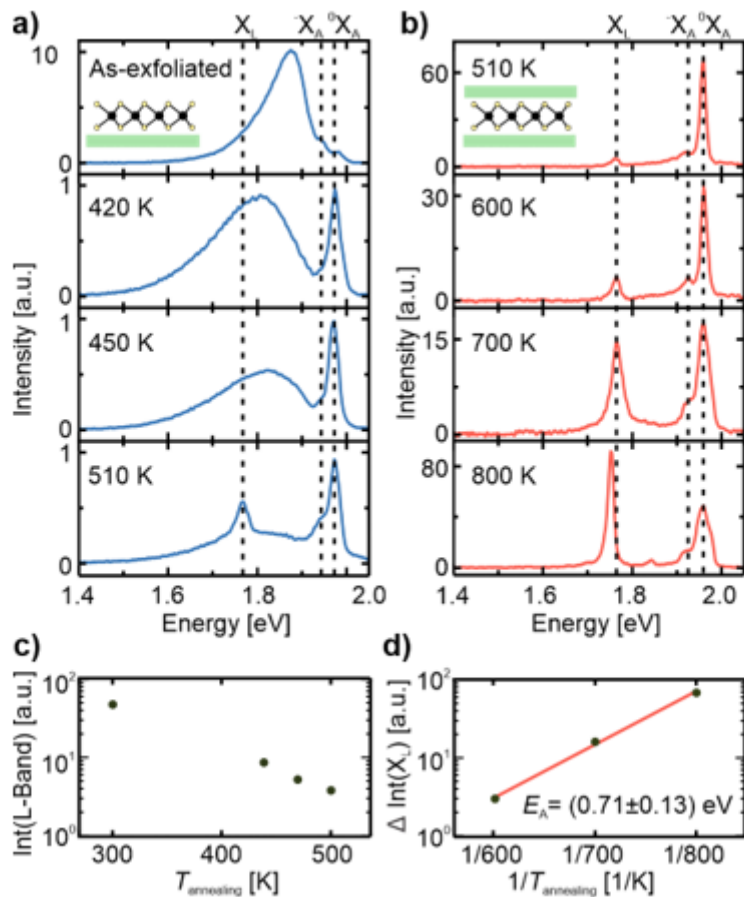


Figure 2

Evolution of MoS₂ low-temperature PL with increasing annealing temperature. a) Compared to as-exfoliated MoS₂ on hBN (top panel) the broad L-band is strongly reduced after successive mild annealing. At 510 K, an emission line XL appears at 1.75 eV (bottom panel). b) PL spectra of fully encapsulated MoS₂. With increasing annealing temperature, the intensity of XL increases. Dashed lines highlight neutral exciton (0XA), trion (-XA), and XL. c) Integrated intensity of the L-band in (a) as function of annealing temperature. The change in L-band emission is related to the desorption rate of adsorbates from the MoS₂. d) Arrhenius plot of thermal defect generation rate extracted from the intensity of XL. The activation barrier is (0.71 ± 0.13) eV consistent with formation of sulfur vacancies.

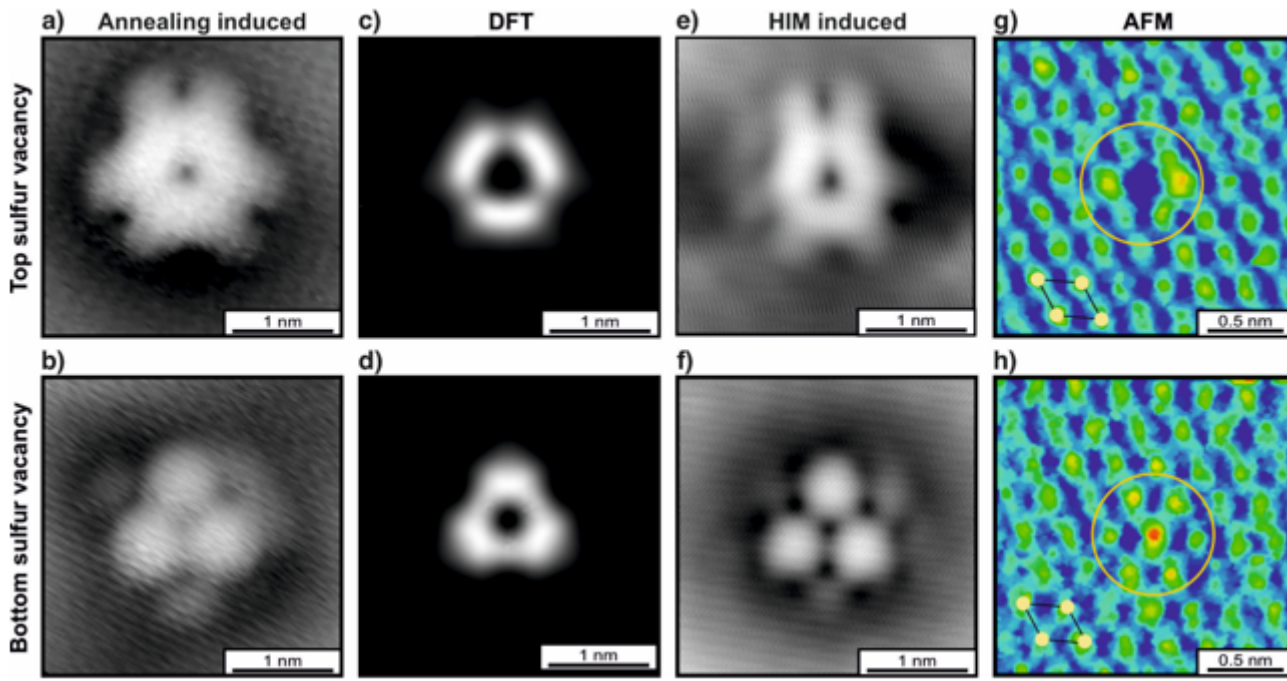


Figure 3

Scanning probe microscopy of sulfur vacancies in single-layer MoS₂ on graphene. a, b) STM images of annealing induced vacancies in the top and bottom sulfur layer. c, d) DFT of 7 x 7 supercell containing one sulfur vacancy. The constant height slice 4.5 Å above and below the MoS₂ layer corresponding to the charge density from sulfur vacancies in the top and bottom sulfur layer, respectively. e, f) STM images of He-ion induced top and bottom sulfur vacancies. g, h) AFM images of the top and bottom sulfur vacancies. The pictogram highlights the sulfur lattice. STM parameters: V_{bias} = 450 mV, I_t = 100 pA.

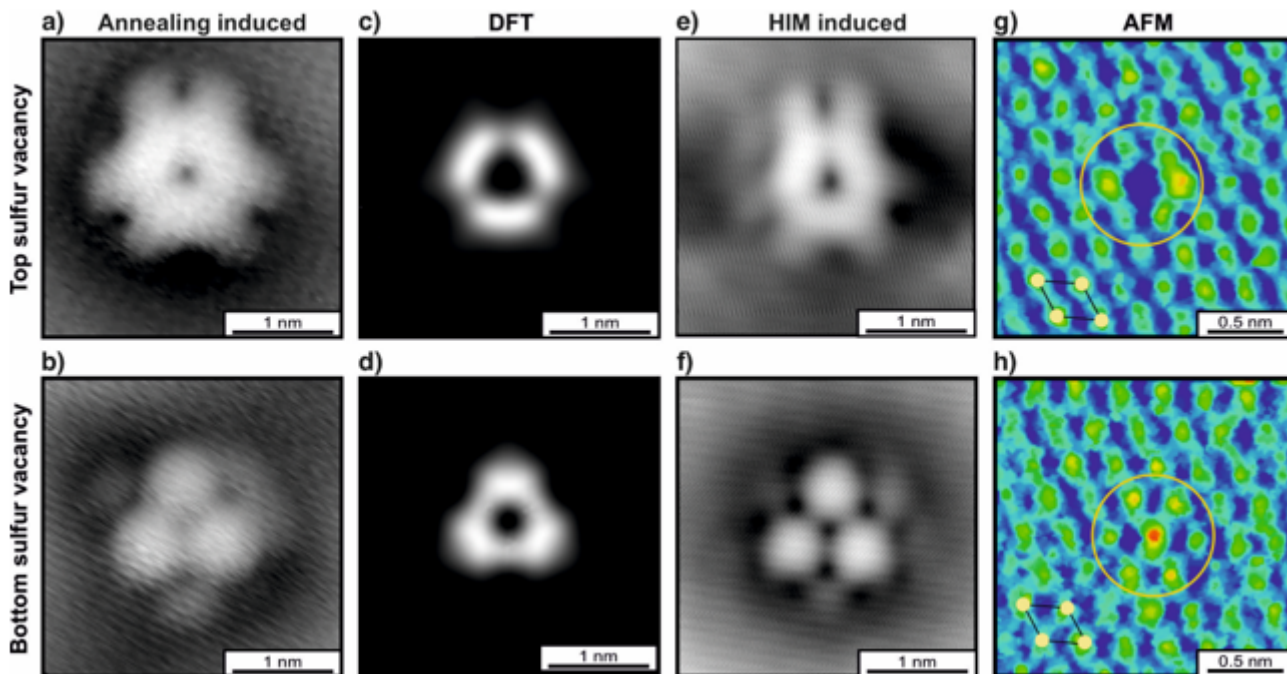


Figure 3

Scanning probe microscopy of sulfur vacancies in single-layer MoS₂ on graphene. a, b) STM images of annealing induced vacancies in the top and bottom sulfur layer. c, d) DFT of 7 x 7 supercell containing one sulfur vacancy. The constant height slice 4.5 Å above and below the MoS₂ layer corresponding to the charge density from sulfur vacancies in the top and bottom sulfur layer, respectively. e, f) STM images of He-ion induced top and bottom sulfur vacancies. g, h) AFM images of the top and bottom sulfur vacancies. The pictogram highlights the sulfur lattice. STM parameters: V_{bias} = 450 mV, I_t = 100 pA.

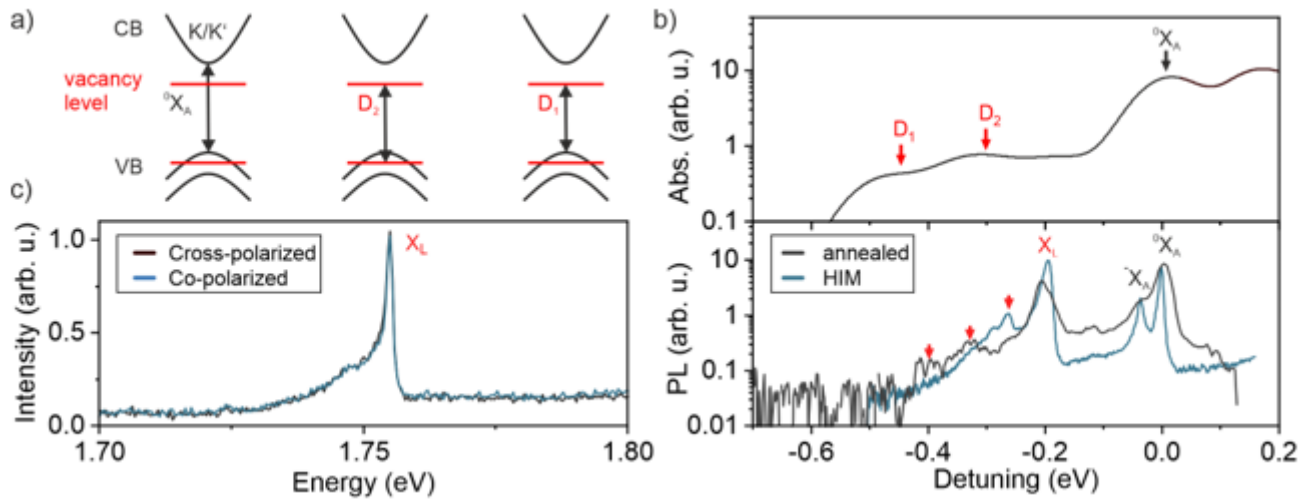


Figure 4

Defect bound excitons in monolayer MoS₂. a) Quasiparticle bands (black) of single-layer MoS₂ with sulfur vacancy levels (red). Arrows highlight the three types of excitonic transitions: between the delocalized bands (0X_A), between the localized defect states only (D₂) and between the valence band and the localized defect state (D₁). b) Calculated absorbance and experimentally detected PL of MoS₂ with sulfur vacancies. All energies are referenced to X_A for better comparison. The absorbance spectrum includes a phenomenological broadening of 100 meV. The most prominent defect emission (X_L) occurs about 0.2 eV below X_A. Further features (red arrows) are resolved at even larger detuning, in qualitative agreement with the broad defect-mediated sub-gap absorbance. c) A single He-ion induced emitter shows no detectable valley polarization (T = 10 K, excitation energy 2.1 eV) as expected for transitions involving only defect levels (D₂).

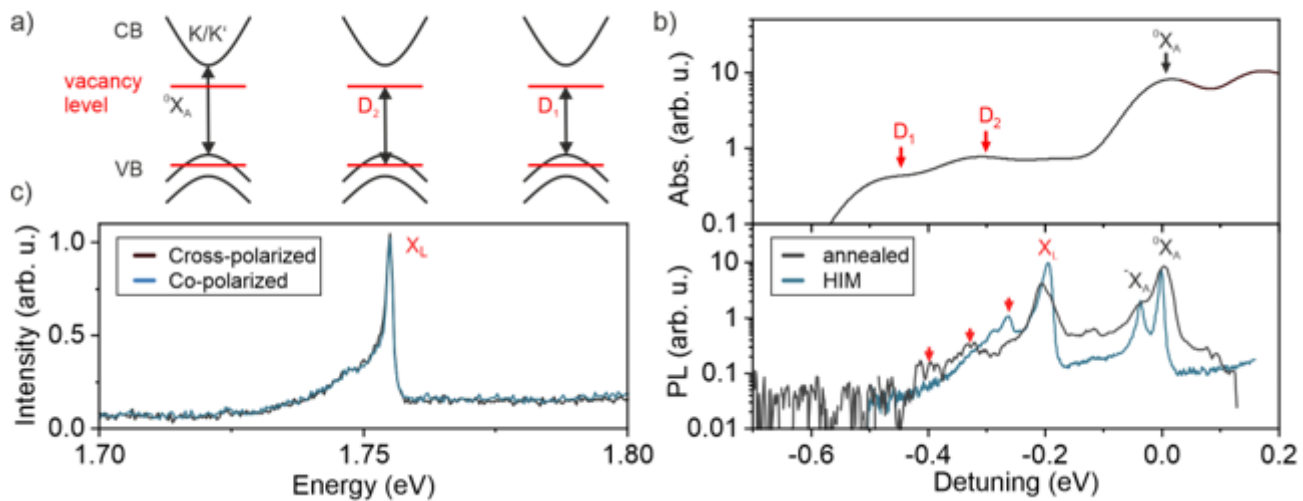


Figure 4

Defect bound excitons in monolayer MoS₂. a) Quasiparticle bands (black) of single-layer MoS₂ with sulfur vacancy levels (red). Arrows highlight the three types of excitonic transitions: between the delocalized bands (0XA), between the localized defect states only (D2) and between the valence band and the localized defect state (D1). b) Calculated absorbance and experimentally detected PL of MoS₂ with sulfur vacancies. All energies are referenced to XA for better comparison. The absorbance spectrum includes a phenomenological broadening of 100 meV. The most prominent defect emission (XL) occurs about 0.2 eV below XA. Further features (red arrows) are resolved at even larger detuning, in qualitative agreement with the broad defect-mediated sub-gap absorbance. c) A single He-ion induced emitter shows no detectable valley polarization (T = 10 K, excitation energy 2.1 eV) as expected for transitions involving only defect levels (D2).

Supplementary Files

This is a list of supplementary files associated with this preprint. Click to download.

- [Mitterreiteretal2020SI20201110.docx](#)
- [Mitterreiteretal2020SI20201110.docx](#)